JGR Planets

RESEARCH ARTICLE
10.1029/2023JE008145

Shallow Water Ice Detection From SHARAD Data in Central Utopia Planitia, Mars

Xiaoting Xu[1,2], Yi Xu[2], Zhuo Han[2], HonKuan Wong[2], Xu Meng[3], Yu-Yan Sara Zhao[1], Roberto Bugiolacchi[2], and Shuanggen Jin[4]

[1]Research Center for Planetary Science, College of Earth and Planetary Science, Chengdu University of Technology, Chengdu, China, [2]State Key Laboratory of Lunar and Planetary Sciences, Macau University of Science and Technology, Macau, People's Republic of China, [3]School of Civil Engineering and Transportation, Guangzhou University, Guangzhou, China, [4]Shanghai Astronomical Observatory, Chinese Academy of Sciences, Shanghai, China

Key Points:

- Water ice content is estimated at 55 vol % to 85% of the material in the center of Utopia Planitia
- Radar results support the formation of Decameter-scale Rimmed Depressions linked to latitude-dependent mantle (LDM) degradation
- We identify the potential presence of a thick icy layer beneath LDM

Supporting Information:

Supporting Information may be found in the online version of this article.

Correspondence to:

Y. Xu,
yixu@must.edu.mo

Citation:

Xu, X., Xu, Y., Han, Z., Wong, H., Meng, X., Zhao, Y.-Y. S., et al. (2025). Shallow water ice detection from SHARAD data in central Utopia Planitia, Mars. *Journal of Geophysical Research: Planets*, *130*, e2023JE008145. https://doi.org/10.1029/2023JE008145

Received 18 OCT 2023
Accepted 22 JUL 2024

Author Contributions:

Conceptualization: Xiaoting Xu, Yi Xu
Data curation: Xiaoting Xu, Zhuo Han
Formal analysis: Xiaoting Xu, Yi Xu, Xu Meng
Funding acquisition: Xiaoting Xu, Yi Xu
Investigation: Xiaoting Xu
Methodology: Xiaoting Xu, Yi Xu, HonKuan Wong, Xu Meng
Project administration: Xiaoting Xu, Yi Xu
Resources: Xiaoting Xu, Yi Xu
Software: Xiaoting Xu
Supervision: Xiaoting Xu, Yi Xu
Validation: Xiaoting Xu, Yi Xu
Visualization: Xiaoting Xu, Zhuo Han, Yu-Yan Sara Zhao
Writing – original draft: Xiaoting Xu
Writing – review & editing: Xiaoting Xu, Yi Xu, Yu-Yan Sara Zhao, Roberto Bugiolacchi, Shuanggen Jin

Abstract One of the key scientific goals of China's first Mars mission Tianwen-1 is to search for ground ice. This study focuses on investigating potential water ice reservoirs in the vicinity of the landing site of the Zhurong rover to provide geological context and references for data interpretation. Our study area is centered on Utopia Planitia (UP), where Shallow Radar onboard the Mars Reconnaissance Orbiter (SHARAD) previously detected subsurface echoes that could be interpreted as ice deposits. Based on the SHARAD data, we have estimated the thickness, dielectric properties, and possible material composition of the surface deposition layer. The inferred water ice volume content ranges from approximately 55%–85%, which is consistent with deposits found on the western edge of UP. Based on morphological features and radar data products, we interpret the detected sediment layer as the latitude-dependent mantle (LDM). We have conducted a comprehensive analysis of the distribution and morphology of various periglacial landforms, including Decameter-scale Rimmed Depressions (DRDs), polygonal landforms, and scalloped depressions on the surface of UP. The implications for the level of degradation are discussed. The radar results provide evidence that DRDs have formed as a result of the degradation of the LDM layer. Additionally, our statistical analysis of concentric crater humps (CCH) linked to subsurface pure glacial ice suggests the possible presence of an icy layer that may be as thick as a kilometer beneath the LDM unit.

Plain Language Summary Potentially large amounts of ice-rich deposits on Mars have been found in the near-surface and subsurface regions at mid-to-high latitudes. One of the key targets for China's first Mars exploration mission "Tianwen-1" was to assess the distribution of buried water ice in the low latitude of the Utopia Planitia region. In this study, we explore the sub-surface structure in central Utopia Planitia and provide a scientific reference for a better geological understanding of the landing area. We focused on an area where interesting radar signals from beneath the surface were detected. Based on these data, we estimated that about 55%–85% of the material in this area could be water ice. We also looked at different surface features in Utopia Planitia, like Decameter-scale Rimmed Depressions, and polygonal landforms. These features helped us understand the level of degradation of groundwater ice in the area. Our analysis showed that certain depressions were formed due to the degradation of a layer called the Latitude-Dependent Mantle. Furthermore, we studied Circular Crater Humps on the surface, the characteristics of which suggest the presence of a thick layer of icy material beneath the mantle. These findings contribute to our understanding of the distribution of water ice on Mars and its potential for future exploration.

1. Introduction

Utopia Planitia (UP) is the largest recognized impact basin in the northern lowlands of Mars (McGill, 1989), centered at ~45°N, ~110°E (Figure 1a). In May 2021, the Zhurong rover of China's first Mars mission "Tianwen-1" successfully landed in the southern part of the UP. The rover carries a ground-penetrating radar instrument aiming to search for ground ice in the middle and low latitudes of Mars with the ultimate aim of preparing for human exploration and settlement (Szocik et al., 2016; Zou et al., 2021). Therefore, understanding the geologic context and water ice reservoir potential of UP is crucial for data interpretation of the in situ exploration mission.

The geologic map shows that the Vastitas Borealis formation (VBF) covers most of UP and consists of the Vastitas Borealis (VB) interior unit and the Vastitas Borealis marginal unit (Tanaka et al., 2005). These units are interpreted to be Late Hesperian (~3.5 Ga) outflow channels water-related sediments (Head et al., 2002; Tanaka

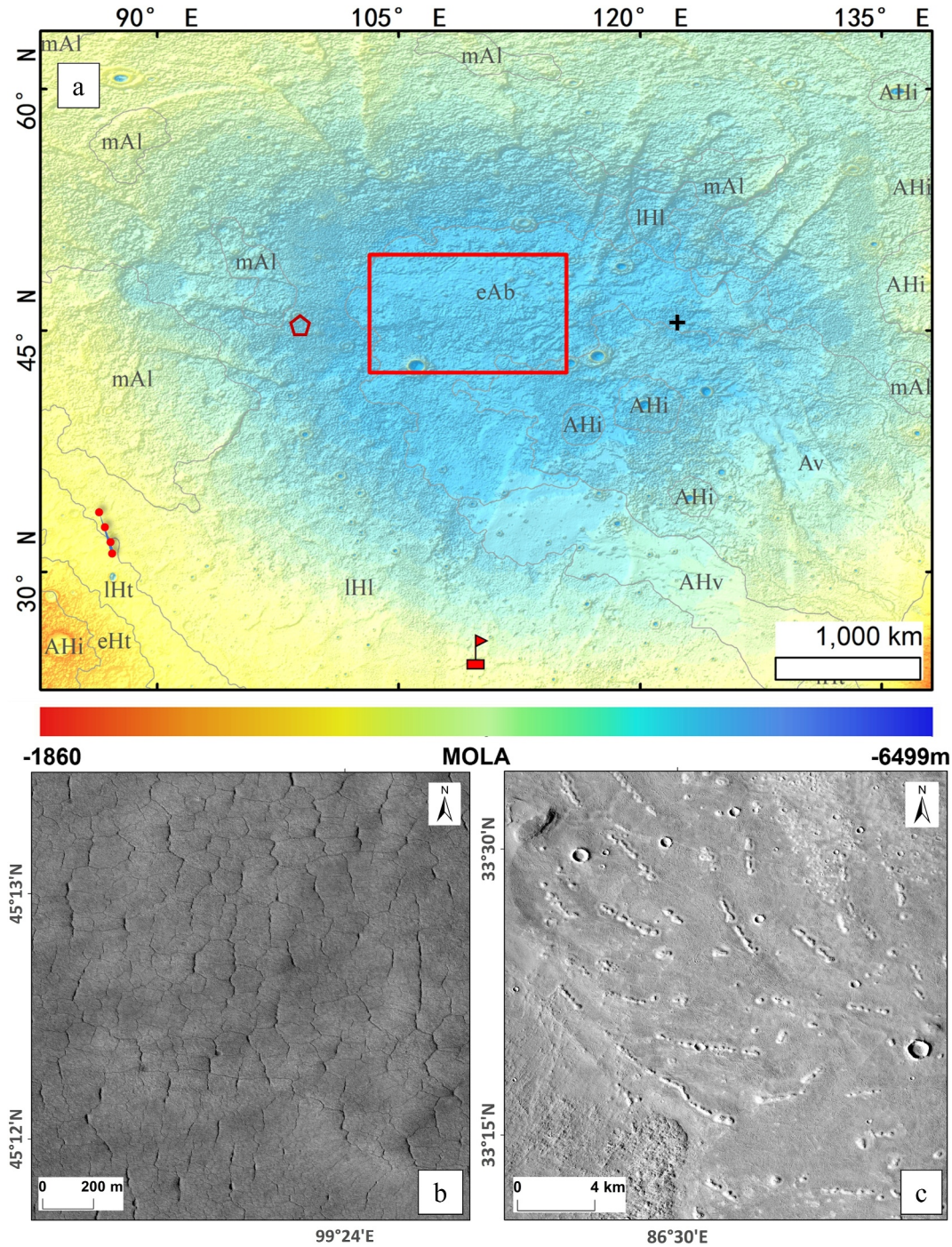

Figure 1. Geological unit map (gray outlines) and some landforms on Utopia Planitia. Panel (a) the red flag indicates Zhurong's landing site. The red square is our study area, and the red polygon, chain-like dots and black cross in panel (a) correspond to the positions of panels (b) and (c) and Figure 6, respectively. The base map is generated with MOLA data. Panel (b) the large polygons on the west of UP from HiRISE and the image No. is ESP_028600_2255_RED. Panel (c) Thumbprint terrain, possible water-related latitude-dependent landforms (Orgel et al., 2019; Séjourné et al., 2019) from CTX and the number is B05_011656_2137_XI_33N273W.

et al., 2005; Werner & Tanaka, 2011) or as a sublimation residue of a large standing body of water (an ocean) (e.g., Kreslavsky & Head, 2002; Parker et al., 1989, 1993). The flow morphology on the VB boundary was formed by fluidized sediments, which are also found in southern UP (Ivanov et al., 2014; McGowan, 2011); Salvatore and Christensen (2014) proposed that the observed landforms result from compaction of muddy units drained from the shallow subsurface of the material inside UP, which appears to be homogeneous at the scale of the mapping. This area hosts both large polygons (closer to the center of the basin) and occurrences of thumbprint terrains (TPT) near the southern edge of UP (as in Figures 1b and 1c), possibly formed by degradation of water-ice sediments (Buczkowski & McGill, 2002; McGill, 1986; Pechmann, 1980). The VBF itself is overlain by the Early Amazonian basin unit (EAb) in the center of UP and the Middle to Late Amazonian Astapus Colles unit around the edge of UP, which is thought to be an icy mantle emplaced as a result of atmospheric precipitation (Skinner et al., 2012; Tanaka et al., 2014).

The Shallow Radar (SHARAD, Seu et al., 2007) has the potential to reveal subsurface structures and detect underground water ice by inverting material properties from radar data. Previous studies by SHARAD suggested the presence of an ice-rich surface layer about 100 m thick (estimated to be 50%–85% water ice by volume) on the western edge of UP (70°–90°E and 40°–48°N) (Stuurman et al., 2016). At mid-latitudes (39°–45°N) in same range of longitude, a thick deposit of material that corresponds to the ice-rich zone has also been discovered with the thickness of 80–100 m and dielectric constant of 3.4–5.3 (Séjourné et al., 2019). These values are consistent with a material that is primarily ice (~50–85% by volume) with some lithic components. Therefore, the edge of UP is suggested to be covered by ice-rich sedimentary units formed in multiple periods. However, a later subband analysis of SHARAD data found a tanδ value of 0.009 ± 0.004, indicating that the material above the reflecting interface may only contain a veneer of near-surface ice rather than consisting entirely of ice-dominated materials (Campbell & Morgan, 2018).

The uppermost sedimentary unit of the layered deposition observed by SHARAD has been interpreted as a latitude-dependent mantle (LDM, 0.4–2.1 Ma; Head et al., 2003; Levy et al., 2009; Mustard et al., 2001; Schon et al., 2012) that formed around 1.5 Ma ago during the late Amazonian period (Séjourné et al., 2019; Stuurman et al., 2016). LDMs are relatively young, successional surface deposits and symmetrically distributed in the northern and southern hemispheres and ranges from 30 to 60 degrees of latitude. Milliken et al. (2003). It is unrelated to the distribution of bedrock (Orgel, C et al., 2019) and appears to be independent of the geological boundaries as mapped by Tanaka et al. (2014). LDMs were ice-rich at the time of formation and their deposition and removal were driven by climate change caused by the tilting of the planet's spin axis (Head et al., 2003; Kress & Head, 2008; Mellon et al., 2004). Stable ground ice extent is related to surface temperature and atmospheric water content, both of which are determined by the climate at the epoch of interest. The atmospheric water content at different obliquities is different: based on evolution theories of orbits and spin axes, the martian climate should have changed significantly even in recent geological history. During the high Mars orbital inclination (Chamberlain & Boynton, 2007), polar ice was transported to mid-high latitudes and formed LDMs (Head et al., 2003). Generally, the layered sediments caused by periodic deposition are composed of eolian dust rich in water ice (Head et al., 2003; Kress & Head, 2008). The LDMs in mid-latitudes are highly sensitive to environmental changes and support the hypothesis of a "water-rich" climate and geologic history (e.g., hydrologic, thermal) (French, 2013; Nelson et al., 2002).

Ice deposited and sublimated when temperatures changed at lower latitudes (Chamberlain & Boynton, 2007; Mellon & Jakosky, 1995), resulting in a landscape influenced by this periodic emplacement and removal. It has been shown that orbital inclination impacts ground ice distribution (Chamberlain & Boynton, 2007), while different solar incidence angles and sediment thickness determine sublimated landforms' morphology (Dundas et al., 2017).

It has been observed that LDMs are associated with strongly dissected terrains (Kress & Head, 2008; Mustard et al., 2001). Hence, some textured terrains on degraded mantle such as polygons or scalloped depressions are thought to indicate debris-covered, ice-rich LDM (Kreslavsky & Head, 2003; Mellon et al., 2008). The dissected area has a large overlap with the whole UP, suggesting the potential presence of ice-rich deposits inside UP. In the center of UP, north of the "Tianwen-1" landing site, various periglacial landforms associated with LDM including Decameter-scale Rimmed Depressions (DRDs) (Bina, 2018) and scalloped depressions (Costard & Kargel, 1995), can be observed on the surface. Other textured landforms include polygonized terrain (French, 2013; Levy et al., 2009), and past and present-day gully activity (Dundas et al., 2015; Malin & Edgett, 2000). These

landforms are similar to those found in periglacial environments on Earth and may indicate the presence of permafrost or a freeze/thaw cycle in the area, which is worthy of attention. SHARAD data have indicated that scalloped depressions and polygons occurring on the surface of western UP are indeed associated with ice-rich material (Séjourné et al., 2019; Stuurman et al., 2016). However, the origin of DRDs remains a mystery. DRDs are widely distributed in the center of UP, and while it is believed that DRDs have similarities with "brain terrain," there are some differences in some key morphological aspects (Bina & Osinski, 2021). Furthermore, there are no correlations with the glacier-related landforms known as lineated valley fill (LVF), lobate debris aprons (LDA) and concentric crater fill (CCF) (Levy et al., 2009; Squyres, 1978, 1979). Therefore, whether a large number of DRDs implies the presence of buried ice deposits in this context needs to be supported by evidence such as radar data (Mangold, 2005; Seibert & Kargel, 2001). The surface deposits that have periglacial landforms (Head et al., 2003; Kress & Head, 2008) scattered across the central UP feature multiple layers similar to LDM. In general, the distribution of the deposits on the edge of the UP is relatively continuous where SHARAD has detected near-surface water ice, and this is more evident at higher latitudes. In comparison, the periglacial landforms in the center of the UP are sparsely distributed.

LDM has been found to consist of at least eight layers by observing steep slopes and impact craters, and previous estimates of the thickness of LDM range from a few meters to tens of meters, and the maximum can reach hundreds of meters (Levy et al., 2009). The thickness of the mesa unit in western UP is ∼100 m as derived from SHARAD data (Séjourné et al., 2019; Stuurman et al., 2016), while the areas with thicker layers occupy a small portion of the global distribution of LDM and are concentrated along the edges of the UP region. For instance, the same layered deposits formed during the Late Amazonian in Arcadia Planitia with widespread excess ice at ∼40°N have an average ∼50 m (Bramson et al., 2015). The thickness of LDM on the edge of UP is also much thicker than the periglacial landforms in the center of UP. Different distribution characteristics and thicknesses of periglacial landforms in the edge and the central region of UP require an investigation of the relationship between the layered mesas in the center of UP and the LDM. Furthermore, the transitions between periglacial landforms could be related to the degradation degree of the icy mantle as a large number of distributed DRDs and polygons are always found together. The thickness distribution of layered mesas and their water ice content variation with latitude, topography and location in UP can be useful to infer the water ice distribution at the southern edge of UP. SHARAD found subsurface reflectors in the edge of UP but did not detect any under the Zhurong landing area for composition analysis. No subsurface echoes have been found in the zone of significant and deep thermokarst (numerous large- and medium-sized scallops at 45°–47°N). One possible reason is that the ice might be sublimated with the formation of scallops in this district. Additionally, the surface roughness may cause scattering of radar signals. For the LDM distributed in the high latitudes (48°–60°N), where it is supposedly widespread and visually thick, interfaces with the underlying basement have not been detected, possibly because SHARAD might be unable to penetrate deeply enough (Séjourné et al., 2019).

In this paper, we focus on the center region of UP, in the same longitude range as the "Tianwen-1" landing site but at a higher latitude where various glacier landforms are widespread (Figure 1). We aim to investigate whether these coverings belong to residual LDM, their water ice content, and thickness distribution, which may help unveil the water ice reservoir condition in the landing region. With elevation data provided by the Mars Orbiter Laser Altimeter (MOLA) and the radar echo signal detected by SHARAD, the thickness, dielectric properties and composition of the material in the study area can be inferred. The distribution and geomorphological characteristics of different forms of glacier landforms have also been analyzed with Context Camera (CTX) imagery data for a better understanding of the evolution and the relationship with the water ice content of landforms. Finally, by combining underground material composition information with relevant surface geomorphic features, we can gain a comprehensive understanding of the geological history and water-ice variations during the Amazonian period in the central region of UP.

2. Materials and Methods

2.1. Data

Visible band data have been used for observational analysis to study the periglacial landforms in our research area: Context Camera (CTX) images from the Mars Reconnaissance Orbiter (MRO) provide context with ∼6 m/pixel resolution and wide coverage (Malin et al., 2007), and the High-Resolution Imaging Science Experiment

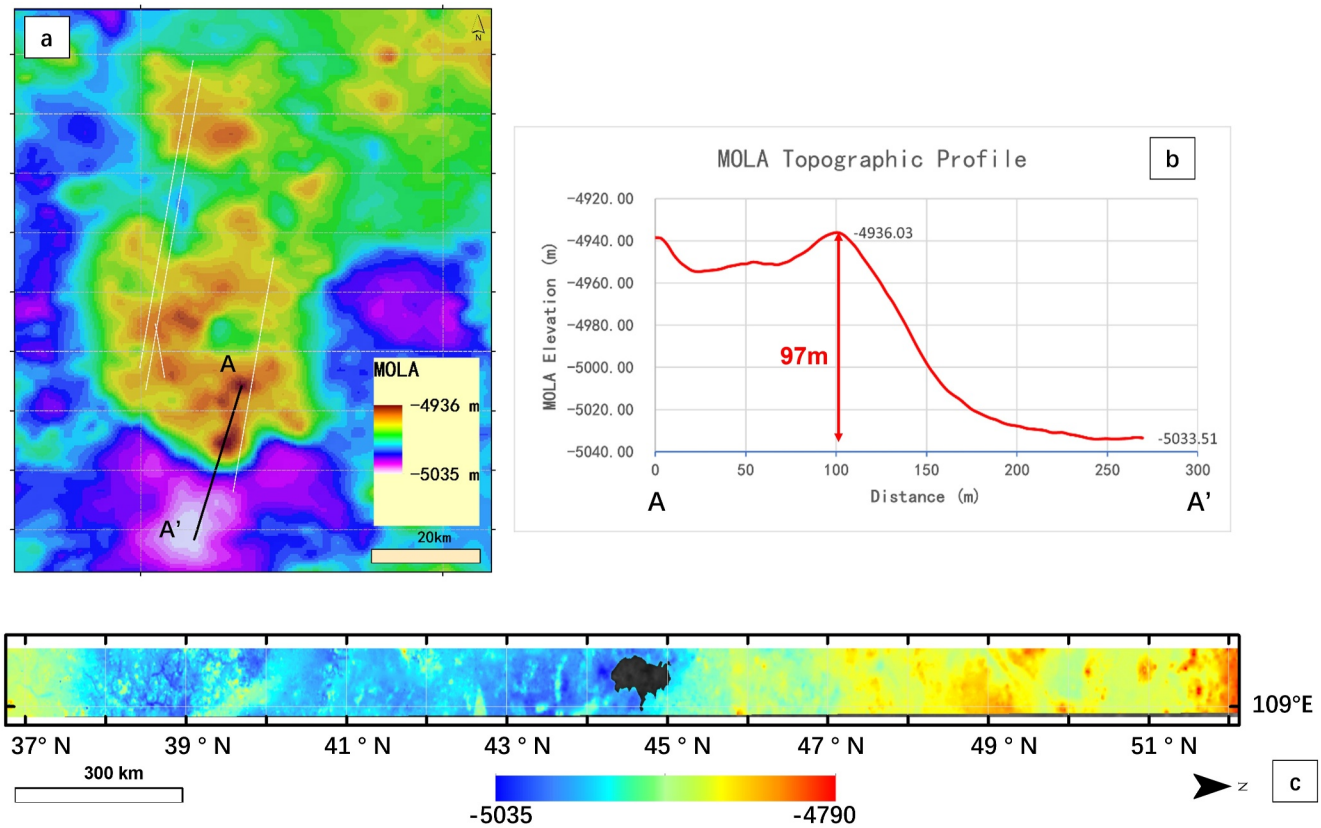

Figure 2. The elevation map of the study area. (a) The elevation map of the area where SHARAD observed the subsurface structures. As indicated by the white lines, the SHARAD data comprises four tracks that indicate the presence of subsurface structures, and from left to right the corresponding radar echo profile is shown in Figures 3a and 3b; Figures S2a and S2c in Supporting Information S1. It is worth noting that the white lines represent portions of the SHARAD ground tracks. Point A is on the top of the mesa with higher terrain while A′ is in the heavily degraded area. (b) The elevation profile from A to A′. (c) The digital elevation model data we used for interpolating the bottom of the study area is indicated by the black color.

(HIRISE) images with a fine spatial resolution of 30 cm/pixel but with limited coverage (McEwen et al., 2007). Figure 4 shows the various periglacial landforms around the study area shown by CTX and HIRISE. SHARAD is a sounding radar provided by the Agenzia Spaziale Italiana (ASI) as a Facility Instrument on the MRO mission. Its center frequency and bandwidth are 20-MHz and 10-MHz, respectively. Vertical and horizontal resolutions are 15 m (free-space) and 3–6 km (cross-track) by 0.3–1 km (along-track), respectively (Seu et al., 2007). Because surface clutters interfere with SHARAD subsurface signals, putative underground reflections are selected when they only exist in radargrams and not in clutter simulations. SHARAD has detected subsurface reflectors in the study region, indicated by the white lines in Figure 2a. The ground track has passed over the layered mesa, which has multiple layers based on surface images, similar to LDM as shown in Figure 2a. Near the southern border of the mesa, there is a severely degraded area A' (Figure 2a). To measure the elevation difference between A′ and A, we used the digital elevation model extracted from MOLA and HRSC with a spatial resolution of 200 m/pixel (Fergason et al., 2017; Laura & Fergason, 2016). To estimate the bottom of the mesa landform in our study area, we extracted the elevation data profile of the surrounding area as shown in Figure 2c. Then, the bottom elevation of the study area was obtained by interpolation. The mesa has an area of 812.42 km^2 and is covered by four orbits of SHARAD (Figure 2a). Two examples of subsurface echoes are shown in Figures 3a and 3c, along with the related clutter simulation plots in Figures 3b and 3d.

2.2. Dielectric Constant Inversion

The dielectric properties of near-surface materials can be inverted from radar echoes and topographic data. First, using the topographical analysis in conjunction with the time delay t of the SHARAD underground reflection, the thickness Δd of the material above the reflection horizon is deduced, c is the speed of light in free space and the

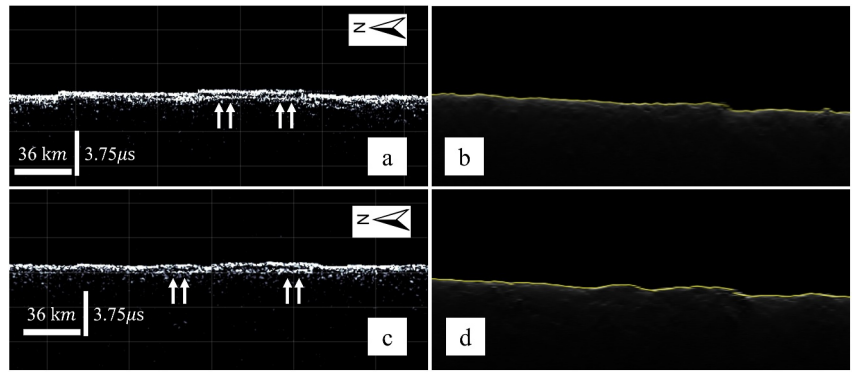

Figure 3. Figures (a and c) are portions of SHARAD echo profiles and b and d are the corresponding equal-scale simulations of clutter, respectively. The track number (a) is 2570502 and (c) is 5583601.

material's dielectric constant ε is determined with Equation 1. The measurement of topographic difference Δd is described in Section 2.1.

$$\varepsilon = (ct/(2\Delta \mathrm{d}))^2 \tag{1}$$

A second inversion method is used to verify the reliability of the results regarding the dielectric constant. The dielectric constant determines the refractive index and reflectivity of the material, and their relationship can be depicted as follows:

$$n = \sqrt{\varepsilon} \tag{2}$$

$$\Gamma = \frac{1-n}{1+n} \tag{3}$$

$$R = |\Gamma|^2 \tag{4}$$

In Equations 2–4, ε is the dielectric constant, n is the refractive index, Γ is the reflection coefficient, and R is the reflectivity. When an electromagnetic wave is incident on a medium, the reflectivity corresponds to the ratio of the reflected wave's amplitude to the incident wave's amplitude. On Mars, the dielectric constant of the polar ice caps is $\varepsilon_{\mathrm{ice}} = 3.15$, and the coefficient of reflection is $\Gamma = -0.275$ (Mouginot et al., 2010). Based on the echo signal on the polar ice cap of Mars, we use Equation 5 to obtain the power of the incident wave A, or the power emitted by the antenna of the orbiter. P is the echo power, P_{ice} is the echo power received from the ice cap, and R_{ice} is the reflectivity of the Martian polar ice caps. By using the emitted energy from the antenna and reflected energy from these surfaces, we can calculate the reflectivity of the study area R.

$$A = \frac{P_{\mathrm{ice}}}{R_{\mathrm{ice}}} \tag{5}$$

$$R = \frac{P}{A} \tag{6}$$

As a result, the refractive index is calculated from the reflection coefficient to obtain the dielectric constant as follows:

$$\Gamma = \sqrt{R} \tag{7}$$

$$n = \frac{1+\Gamma}{1-\Gamma} \tag{8}$$

$$\varepsilon = n^2 \tag{9}$$

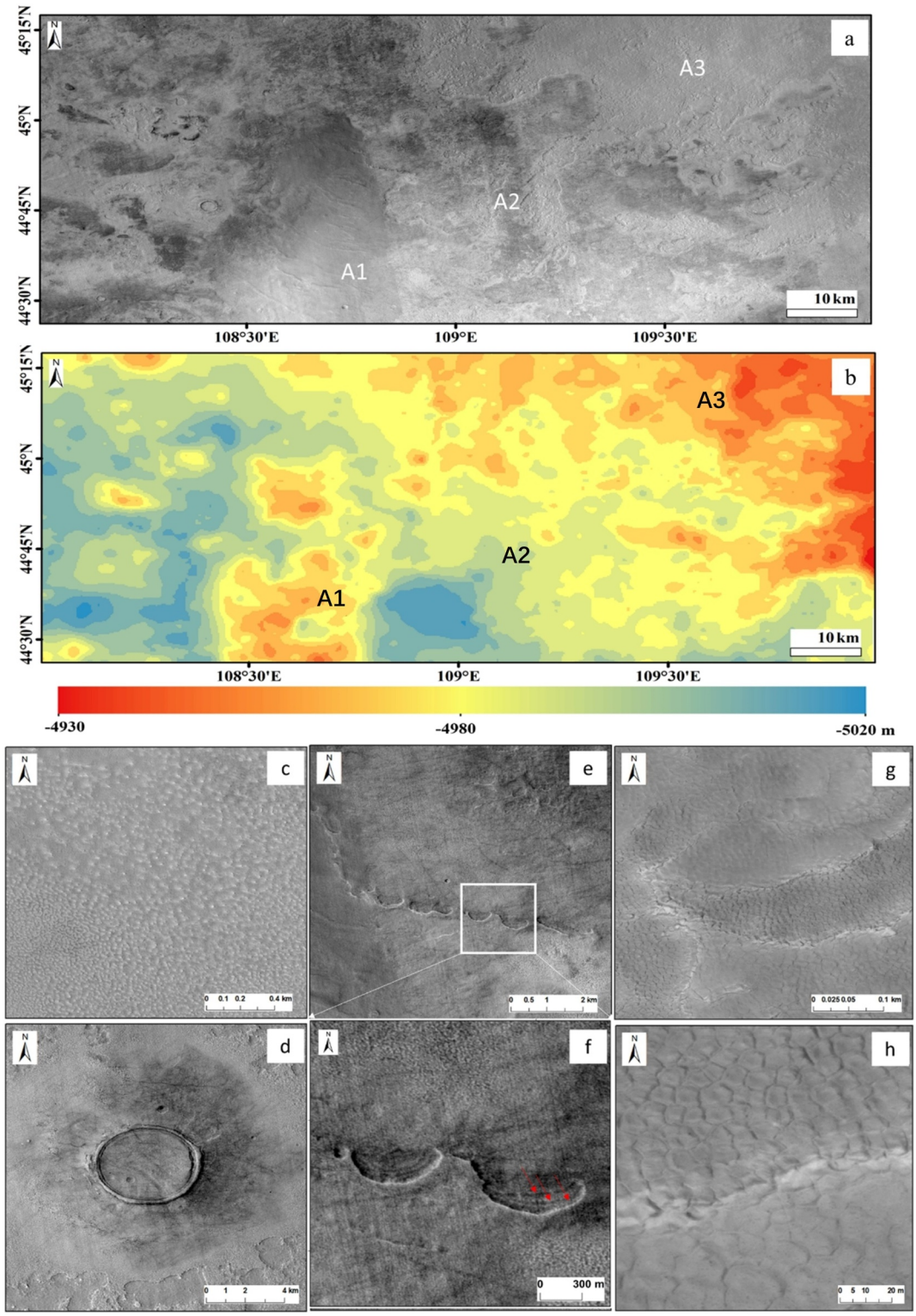

Figure 4. Periglacial landforms in the study area. (a) The three-layer mesa A1, A2, A3 be showed from Murray-Lab_CTX-Mosaic_beta01_QuadMap. (b) The digital elevation model based on MOLA and HRSC with a spatial resolution of 200 m/pixel. (c) Decameter-scale Rimmed Depressions (DRDs), from HiRISE No. is ESP_027360_2250_RED. (d) Concentric crater hump (CCH), from CTX No. D01_027426_2245_XI_44N252W. (e) The boundary of the mesa defined by a series of scallops. (f) An enlarged view of the white square in (e). (g) The polygonal landforms that are commonly encountered on the mesa, and (h) the enlarged view of (g). Panels (a), (e), and (f) are all from CTX No. Murray-Lab_CTX-Mosaic_beta01_E108_N44. Panel (g) and (h) are from HiRISE No. ESP_026727_2255_RED.

2.3. Loss Tangent Inversion

Calculating the loss tangent of this layer can also help constrain the material composition (Campbell et al., 2008). The average value of the loss tangent of the mesa material is estimated by obtaining the energy attenuation of the electromagnetic wave from the surface to the subsurface echo point, or the power ratio between the surface and subsurface echoes. The surface echo power P_s and subsurface echo power P_{ss} can be expressed as follows using the approach suggested by Porcello et al. (1974) and Orosei et al. (2017):

$$P_s = P_t\left(\frac{G\lambda}{8\pi H}\right)^2 |R_S|^2 L_s \tag{10}$$

$$P_{ss} = P_t\left(\frac{G\lambda}{8\pi(H+z)}\right)^2 \left(1-|R_S|^2\right)^2 |R_{ss}|^2 \times \exp(-2\pi f \tan\delta t)\, L_{ss} \tag{11}$$

$$\ln\left(\frac{P_{ss}}{P_s}\right) = -2\pi f t \tan\delta + K \tag{12}$$

where G is antenna gain, P_t represents transmitted power, H represents spacecraft altitude, λ is the wavelength, z represents layer thickness, and f represents radar frequency. L_s and L_{ss} are the general roughness loss terms at the surface and subsurface interfaces, and t has been defined in Equation 1. R_s is the surface reflection coefficient and R_{ss} is the subsurface reflection coefficient in Equation 11. Equation 12 is produced by taking the natural logarithm of Equation 11 divided by Equation 10. The tan δ in Equation 12 only depends on the slope between ln (P_{ss}/P_s) and $2\pi f t$. The reflection coefficients, and roughness losses at the subsurface and surface interfaces determine the constant term K.

3. Results

3.1. Periglacial Landform

The textured terrains associated with LDM are nearly ubiquitous in the mapping strip for our study area, as shown in Figure 4. SHARAD detected a subsurface structure in area A1 (Figure 4a) where the layered mesas are located, standing higher than the surrounding terrain (Figure 4b). The surface of the mesa in this area is smooth and surrounded by various textured landforms: scalloped depressions (Figures 4e and 4f), small polygons (diameter <25 m) as shown in Figures 4g and 4h, and a large number of DRDs (Figure 4c) distributed in lower terrain around the mesa. Our study area (a) in Figure 4a is tens of meters higher than the surrounding terrain, as derived from MOLA data. LDM was found to consist of at least eight layers, the thickness for each ranging from several meters to tens of meters (Kress & Head, 2008). In Figure 4a, area A1 is overlaid on another layer of sediment A2, while area A3 appears to be below the layer A2. The geomorphologic difference between areas A1 and A2, A3 is that the two lower mesa units all have DRDs and ice-edge landforms such as polygonal and scalloped depressions. DRDs appear together with the polygonal landforms and no obvious boundary exists between these two landforms. Scalloped depressions that are joined end to end form the boundary of a single mesa (Figure 4e). Some scalloped depressions also appear on the surface of the mesa.

The textured landforms in this area include DRDs and polygonal landforms (Figures 4c and 4h). There are three main morphologies of DRDs that underwent thermal contraction and differential degradation: ellipse, labyrinth, and teardrop (Figure 6, Bina & Osinski, 2021). These features are small-scale depressions surrounded by narrow rims that are no more than a few meters in width and stand at a higher elevation relative to the surrounding terrain. They all appear around the mesa in our study area (Figure 5), that is, where the mesa has been degraded and removed (Bina & Osinski, 2021). Figure 6 shows the coexistence and interconversion of various types of DRD landforms.

We mapped periglacial features associated with LDM in the study region with CTX and HiRISE images (Figures 4c–4g). The distribution of the topmost mesa is shown in the blue area (Figure 5) and is dispersed as a result of degradation. DRDs are closely related to the distribution of polygons but appear below the latitude of 48°N. In addition, DRDs never appear on the surface of the topmost mesa. Polygons also occur in the north part of the study area up to 50°N, and they almost disappear along with the dispersed topmost mesa. The small-sized (~≤25 m in diameter) polygons can be observed on the surface of the mesa in our study area, which may be

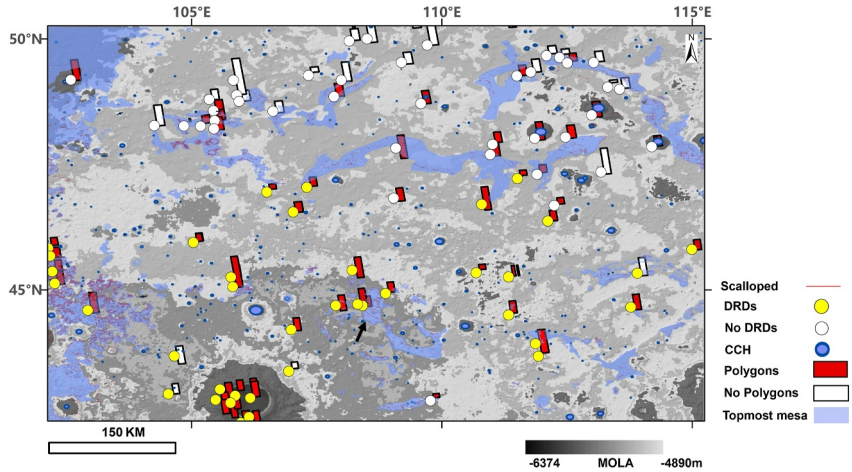

Figure 5. Periglacial landform distribution map. The black arrow indicates the blue area where SHARAD observed the subsurface, and the blue area indicates the uppermost mesa based on CTX that is consistent with this area. On the CTX, we outlined the scalloped depression with curved lines. We tallied the number of polygons and DRDs on all available HiRISE images in the study area.

associated with thermal contraction cracks in fine-grained cohesive materials (e.g., Levy et al., 2010; Ulrich et al., 2010). Scalloped depressions are not confined solely to the uppermost mesa, but they are also observed on its lower surface and edge, as depicted in Figure 4a(A2). Furthermore, as illustrated in Figure 4d, they manifest within the ejecta blanket of the crater and along the inner crater wall. Notably, scalloped depressions are not limited to the polygonal terrain but also extend into the domain of the DRD. Within our study area, when neither DRD nor polygonal features are present across the entire area, scalloped depressions do not manifest. In other words, scalloped depressions have upper and lower boundaries at approximately 40–50° latitude.

There are many similarities between mesas and periglacial features associated with LDMs, including layered structures, surface textures, and thickness measurements derived from MOLA data. We speculate that the mesas are remnants "LDMs" that have gone through the degenerative stages (Schorghofer & Forget, 2012; Orgel et al., 2019).

3.2. Concentric Crater Humps

In the study region, a unique type of impact crater that has a hump on the interior unit of the crater is found, which we call the concentric crater hump (CCH). The landform seems to be only present in the center of UP, as shown by blue circles in Figure 5. It has a ring-shaped outline and a center area higher than the crater rim (Figure 7a). The

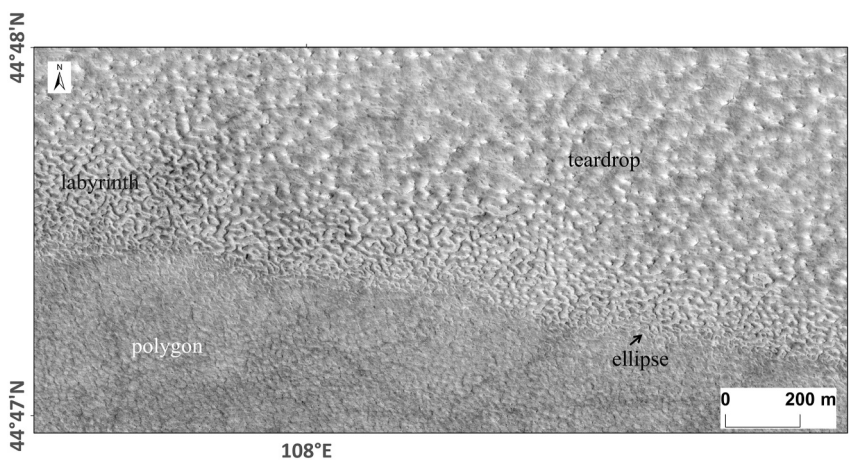

Figure 6. Three types of transitional landforms on DRDs from HiRISE No. ESP_027360_2250_RED.

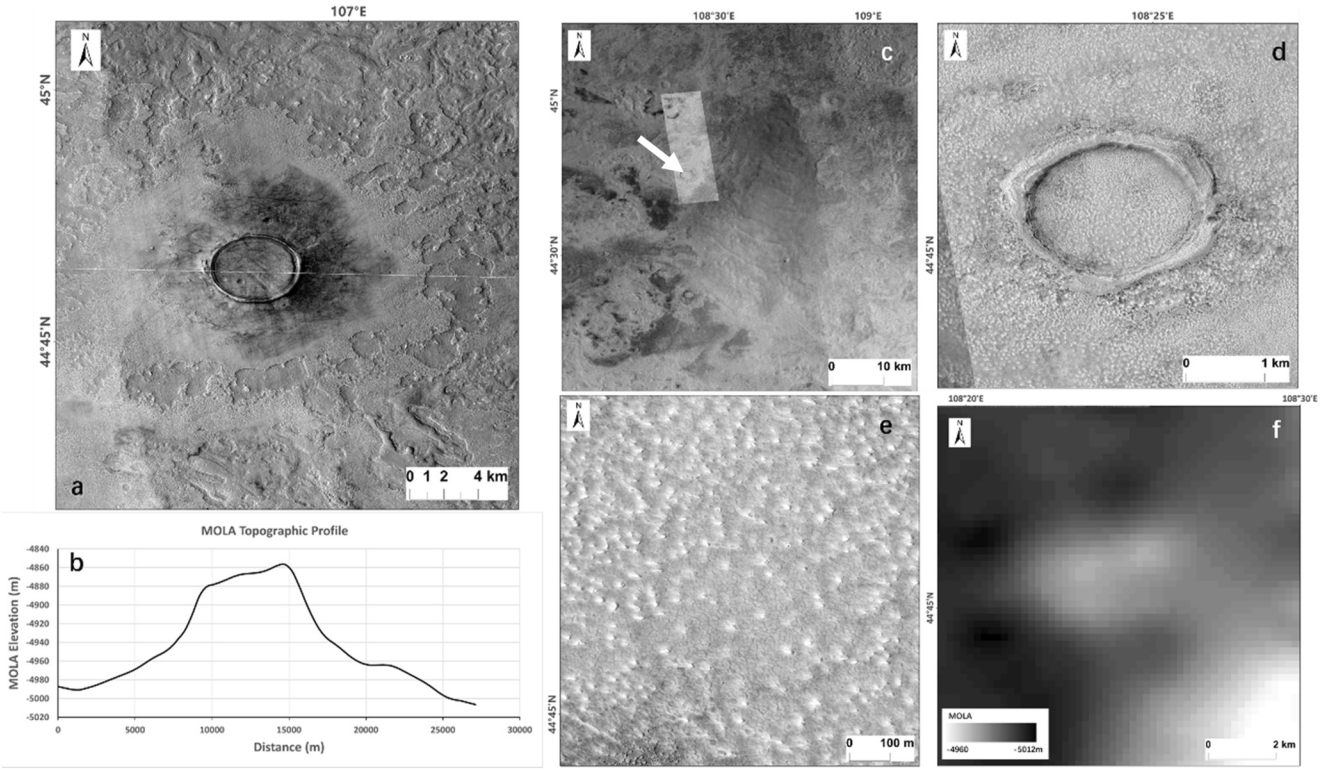

Figure 7. The morphology diagram of CCH. Panel (a) shows the host impact crater and the inner hump filled from CTX No. D01_027426_2245_XI_44N252W. Panel (b) the profile of the crater from MOLA, and the location is indicated by the white line in panel (a). Panel (c) is from CTX No. Murray-Lab_CTX-Mosaic_beta01_E108_N44. Panel (d) is the enlargement of the white arrow on (c) d is a CCH that has a more severe degradation than (a). Figure (e) is the bottom of the crater in Figure d, we can see the DRDs and some small polygons. Figure d and e are all from HiRISE No. ESP_027149_2250_RED. Figure (f) is the MOLA data of (d).

ejecta blanket is covered by various periglacial landforms. As a result of degradation, the morphological features of the crater floor are different from the characteristics of CCF (Levy et al., 2009). CCF usually shows brain terrain texture and concentric deformation on the surface. CCHs' inner elevation is tens of meters higher than the surrounding terrain. In Figure 7a, scalloped depressions can be observed on the ejecta blanket and the degradation level increases toward the center. In Figure 7d, the ejecta blanket has been almost completely degraded and a few polygons and DRDs appear on the crater floor (Figure 7e). We can still observe the hump over the surrounding flatland in the elevation image (Figure 7f). The topographical characteristics of the CCH have not disappeared despite the severe degradation indicated by DRDs and it can be distinguished from other craters by this feature.

Due to the absence of obvious depression in the interior of the crater, the formation of CCH might be different from CCF. CCF was formed by a debris-covered glacier-like process (Levy et al., 2009), whereas the infilling material of the CCH might mostly be sourced from the ice-rich material by the impact or other water-related factors. In this type of crater, the crater pit and eject blanket are under permanent cover. Polygons, DRDs and a few scalloped depressions appear on the surface of this layer, while deeply degraded CCHs only contain DRDs as illustrated by Figure 7b. However, the MOLA data (Figures 7b and 7f) show the CCH's profile to be humpy and, most probably, not related to its degradation degree. Is this to indicate that this profile was formed during the impact rather than covered and filled afterward? In other words, its hump cannot be caused by filling. The periglacial landforms on the surface of CCHs are similar to those on the mesa, both in terms of type and degradation level. CCHs appear in geological units older than the uppermost LDMs, especially in the center of the UP where we found subsurface structures detected by SHARAD. Therefore, although we cannot detect the same sub-structure from SHARAD data, as in Figure 3, we can estimate that it is likely that the surface material of the CCH is represented by LDM.

We calculated the crater-size distribution in our study area (blue circles in Figure 5). The diameters of CCHs extend from ~230 m to 9.9 km, and most are within the 200 m–1.5 km range (Figure 8). A depth-diameter analysis

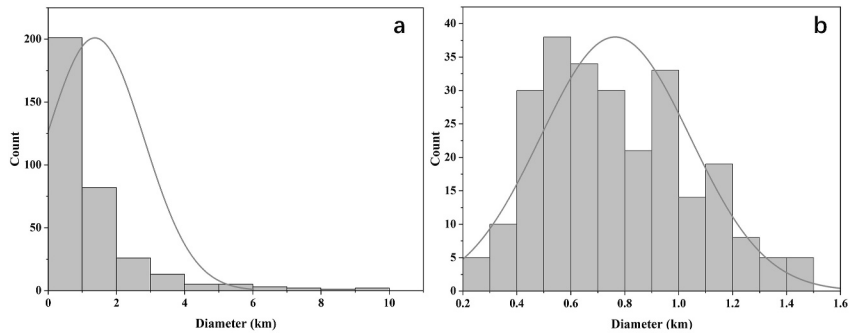

Figure 8. The diameter distribution of CCH in the study area. Panel (b) Distribution chart for diameters less than 1.5 km.

indicates that water ice was previously buried at a depth of tens of meters, maybe even hundreds of meters. It is worth noting that CCH does not appear on the uppermost mesa. From the degree of degradation, CCH is on the lower terrain and more degraded than the right LDM (Figure 7c), implying that it predates the topmost LDM.

3.3. Dielectric Constant Results

In Figure 2c, the black area represents the underground structure detected by SHARAD, and its thickness ranges from ~58 to 130 m based on the interpolated base elevation (Figure 9c). In the first step, we selected data points with clear surface reflectors and subsurface reflectors. To mitigate the uncertainties caused by surface roughness, the data points with wide width at half maximum (FWHM) are filtered out. In this work, we choose the threshold value of FWHM is 220 ns (Figure 9a). The orange data in Figure 9a are those with qualified pulse widths, corresponding to the black-colored tracks in Figure 9c. The selected data correspond to the area of thickness greater than 76 m (Figure 9b). Based on the thickness of the strata and the time delay of the subsurface echo from SHARAD, we obtained the average dielectric constant to be $\varepsilon' = 4.15 \pm 0.04$. The range of the estimated dielectric constant is 2.6–5.4 with Equation 1. The inversion results of the dielectric constant are also in this range of 3–4.5 (red square in Figure S1 in Supporting Information S1). Since the dielectric constant of water ice is 3.15, it is reasonable to speculate that the material contains ice-rich deposition.

The loss tangent value is calculated using the slope of the best fitting line $\ln(P_{ss}/P_s)$ and $2\pi ft$ as shown in Figure 10. The initial constant term is the intercept of the best-fitting line with the Y-axis, listed in Table 1, and the mean loss tangent value is 0.0052. This is consistent with ice-rich deposits (Campbell & Morgan, 2018).

We assume that the deposits consist of water ice ($\varepsilon_{H_2O} = 3.15$), lithic material with a relative permittivity of 8, and pore space (Kreslavsky & Head, 2002). As shown in Figure 11, the potential composition of the deposited material can be inferred using the three-phase power relation developed by Stillman et al. (2010). According to Viking landing site measurements, the surface porosity of loose wind drift material on Mars is approximately 50% (Moore et al., 1987). In this paper, we adopt the value of 50% as the upper limit for the porosity. Based on the relative permittivity of the materials ranges from 2.6–5.4, so the contour line shows that the content of water ice is 55%–85%, the results are consistent with a material that is primarily ice with some lithic components. Further, previous studies on the western edge of UP have shown similar results and interpreted that the deposits are analogous to LDM (Séjourné et al., 2019; Stuurman et al., 2016).

4. Discussion

4.1. Water ice Content in the Center of UP

From the dielectric properties results and geomorphologic evidence, three units A1-3 in Figure 4a are interpreted as LDMs formed at different periods of high obliquity. The three-layer LDM experienced different degrees of degradation when the orbital inclinations were low. Different periglacial landforms are distributed around the area where subsurface echos are detected by SHARAD. These phenomena are consistent with the LDM; its distribution is accompanied by ice-rich sediments that may have existed in relatively recent time (Costard & Kargel, 1995; Soare et al., 2008). The average thickness of LDM in our study area is consistent with previous estimations ranging from a few meters to tens of meters with a maximum value of hundreds of meters (Levy

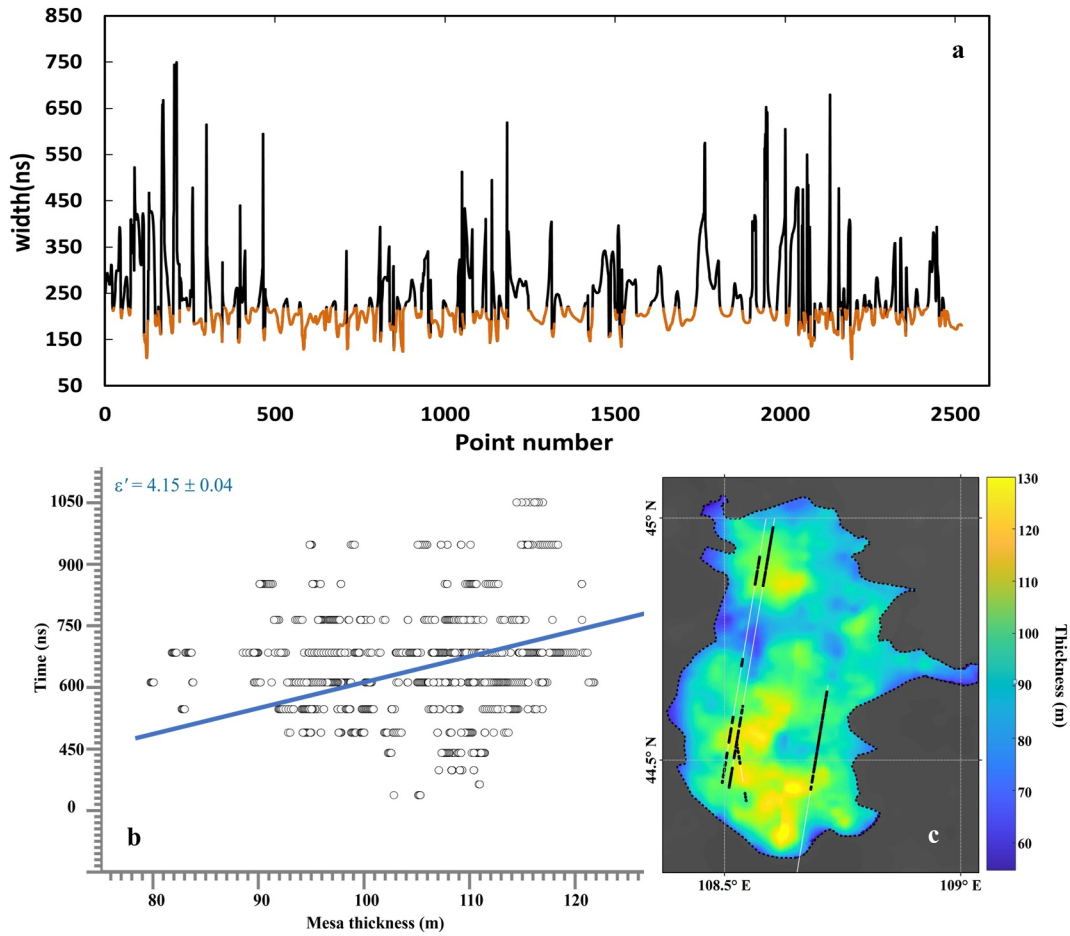

Figure 9. The thickness of mesa in the study region. Panel (a) shows the pulse width at -3 dB of the SHARAD points. Panel (b), Dielectric constant regression results. Travel time versus layer thickness is plotted. Based on the slope of the blue line, the dielectric constant is 4.15 ± 0.04. The dielectric constant represents the average dielectric constant measured at all locations in which layer thickness measurements could be made (see supporting information). Panel (c) is the interpolation of the calculated thickness results of the substructure from SHARAD in our study area.

et al., 2009). The thickness of the sediment is up to 130 m in the study region, but the mesas are sparsely distributed in the center of UP, indicating different degradation rates or accumulation rates after freezing/sublimating cycles in the center region and the edge part of UP. SHARAD data only show distinct and clear subsurface echoes deeper than 76 m in the study area. The subsurface reflectors become blurred and even disappear when the LDM becomes thinner. The reason that the LDM at the lowest elevations of UP is more dispersed and degraded to a greater degree than at the edge may be because when considering both surface heat and atmosphere, the temperature depends on altitude rather than latitude, leading to a greater degree of degradation in low elevation areas (Jakosky et al., 2017; Wordsworth et al., 2013). This may explain the question raised by Stuurman et al. (2016), if these are indeed LDMs, according to the distribution why there are no subsurface structures found in other districts. Although SHARAD only detected distinct subsurface echos deeper than 76 m in the study area, the mesa unit is assumed to have a similar composition. The average dielectric constant is $\varepsilon' = 4.15 \pm 0.04$ (Figure 9b), and the average loss tangent 0.0052 (Table 1), the water ice content can reach 55%–85%. This dielectric constant is similar to those reported by Stuurman et al. (2016), while the estimated average loss tangent value is comparatively lower than the one obtained by Campbell and Morgan (2018) in UP. This may suggest that the ice content in central UP is higher than that in the edge region. The LDM unit is composed of multiple layers, and the degradation degree of the LDM layer varies both regionally and temporally depending on atmospheric pressure and temperature. For instance, the ice-rich strata in the northwest of UP are currently noticeably thick, whereas those at lower latitudes have undergone significant degradation. Additionally, the LDM layers formed at

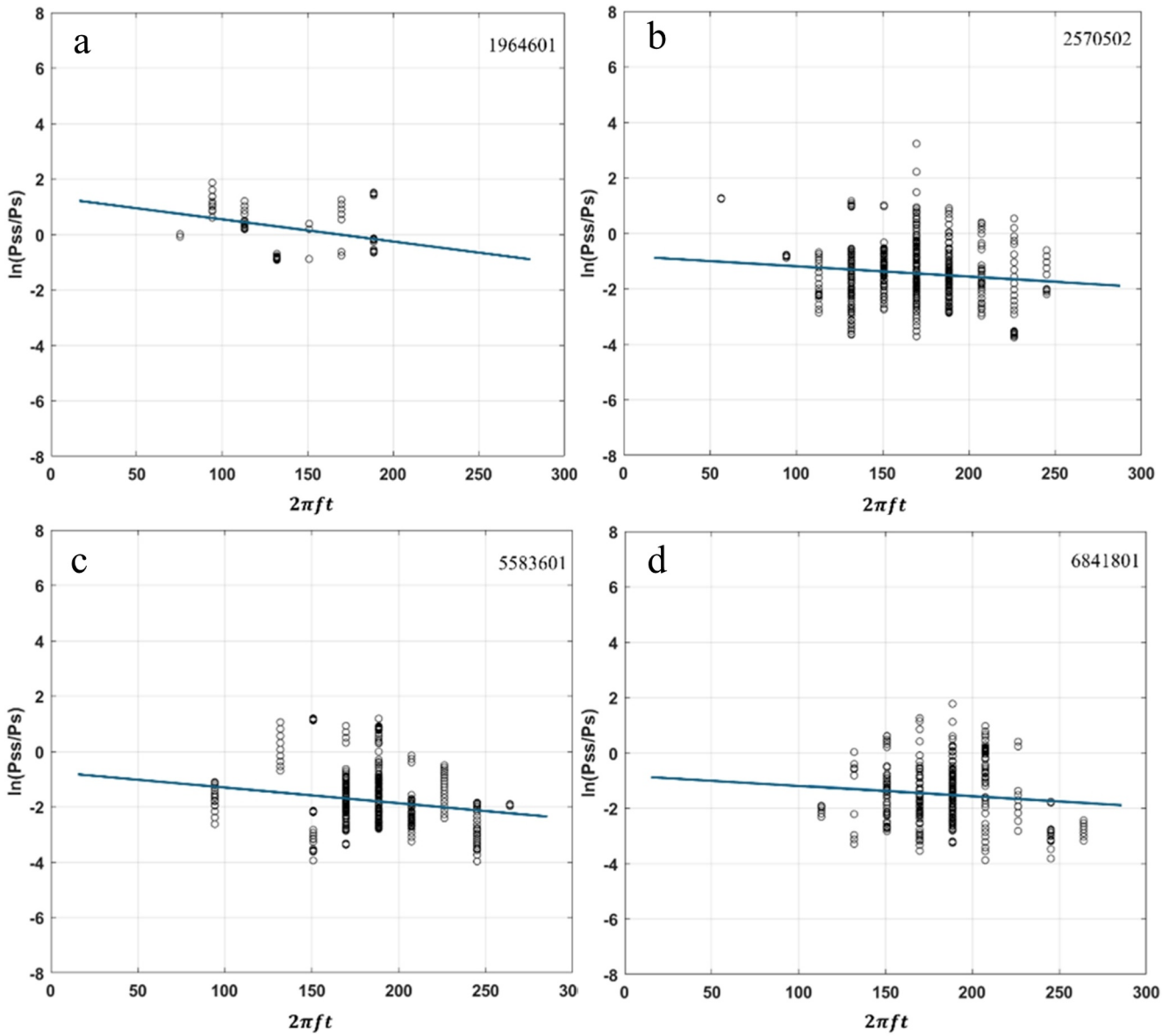

Figure 10. Graph of natural logarithm on subsurface-surface echo power ratio versus The track numbers listed in Table 1 cross on our study region in the Utopia center. The best-fit lines are computed by using a linear regression. Figures (a–d) correspond to SHARAD observations 1964601, 2570502, 5583601, 6841801, respectively.

different periods exhibit various types of periglacial landforms. Consequently, the material components, such as the water ice fraction, vary among these layers (see Sections 4.2 and 4.3 for more details). It is reasonable to assume that the surface layer contains a higher water ice content compared to the underlying layers, as it was formed more recently and has undergone less degradation.

Table 1
Coefficients of the Best Fit Lines for Loss Tangent, Together With Their 95% Confidence Bounds

Track number	Loss tangent and the 95% confidence interval	Constant term (K) and the 95% confidence interval
1964601	0.0079 [0.0023, 0.0130]	1.343 [0.5327, 2.1530]
2570502	0.0036 [0.0016, 0.0057]	−0.8225 [−1.1740, −0.4708]
5583601	0.0057 [0.0028, 0.0087]	−0.7261 [−1.2810, −0.1708]
6841801	0.0038 [0.0004, 0.0080]	−0.788 [−1.5800, 0.0036]

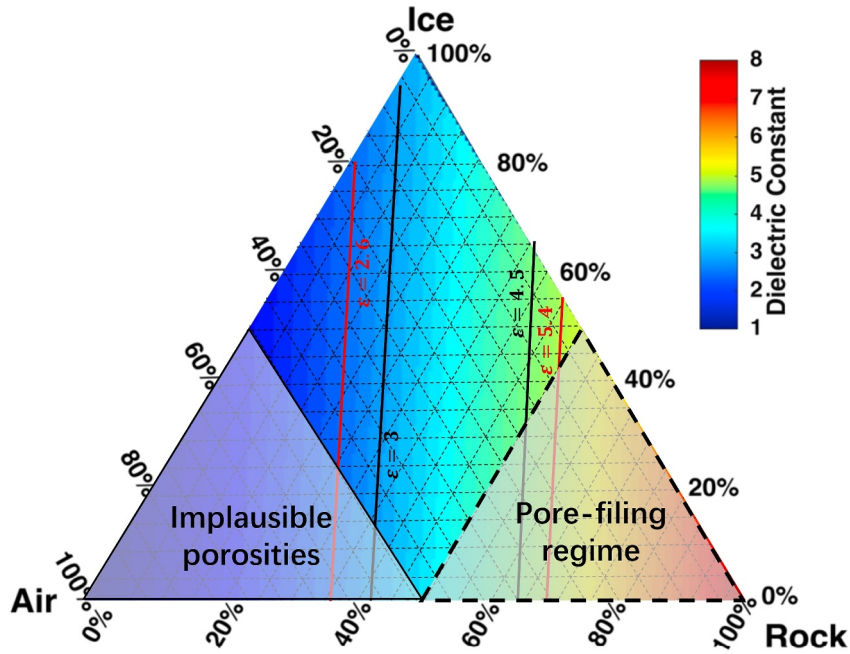

Figure 11. The ternary diagram on relative permittivity calculations for a mixture of ice, rock and air (Moore et al., 1987). The black lines are the result of our inversion of the dielectric constant 3–4.5, and the red lines are from formula 1, 2.6–5.4.

Almost all craters that appear at the lowest elevations of UP are buried impact craters that have no obvious outlines of ejecta blankets. Since the study area is an eAb unit (Tanaka et al., 2014), the strata where these impact craters are located date from the Early Amazon period at the Latest. In contrast, the mesa in Figure 4a has almost no impact craters on A1-3, which suggests that the mesa is relatively fresh; consequently, the water ice-rich covering material we found must have formed later than the early Amazon. The area with subsurface structures discovered by SHARAD is consistent with the platform area outlined with the MOLA data in Figure 2a and CTX imagery data in Figure 4a-A1. According to the image data of the mesa and its surrounding areas, the thickness and layering and various Periglacial landforms appearing on the surface are very similar to the characteristics of LDMs, which experienced degradation.

Our analysis results of the radar data are relatively consistent with the thickness and material composition of the platform discovered on the northwest side of UP by Stuurman et al. (2016), and the two study areas are in the same latitude zone. We speculate that these platforms are very likely due to orbital inclination driving the formation of a global multi-layered water-ice-rich blanket at mid-to-high latitudes. Therefore, in summary, it is inferred that the mesa represents the remnant of the LDM that formed in the past few million years and subsequently experienced degradation.

CCH craters appear on the terrain older than the uppermost LDM. Unfortunately, the timing cannot be estimated due to the absence of craters on the ejecta of CCH, possibly caused by the fast obliteration speed of small craters on the ejecta material. No obvious difference between the surface morphology of CCH and the surface of LDM is found. CCH is similar to the Ring-mold craters (RMCs) proposed by Kress and Head (2008), who interpreted the unusual morphology of RMCs to be the result of the impact into a relatively pure ice substrate below a thin regolith. Hence, the formation of CCH might be related to the subsurface water ice. Based on the distribution results of excavation depths of CCHs in the studied region, the previous ice-rich layer might be below a 20 m thick crust and reach hundreds of meters or even kilometers in thickness. Considering the low topography of this region and its central location within the basin, there is a possibility of the accumulation of a significant amount of water ice materials during the Early Amazonian period. However, due to the unconstrained thickness of the eAb unit, it is unclear whether the icy layer extends to the underlying VBF unit. The eAb unit is not present at the Tianwen-1 landing site and could have been removed due to increased surface temperature in low latitudes or the deposition of eAb only occurring in the center region of UP as CCH is not present in the southern edge of UP.

4.2. Scalloped Shape

The scalloped shape (Figure 4e) of the LDM formation due to the sublimation of ice-rich materials is assumed to represent a thermokarst landform (Dundas et al., 2017). Three sub-parallel ridges and pole-facing scarps in the same depression are common in UP. For instance, there are parallel ridges of the scallops on the topmost mesa as shown in Figures 4a(a) and 4f. These scallops contain evidence of three main periods of ice instability (Dundas et al., 2017). The development of scalloped depressions as sublimation-thermokarst landforms is explained by a simple model for climate variation with obliquity. There is a tendency for scallop expansion to occur at low obliquity at midlatitudes, and interior structures consisting of arcuate ridges can be formed as a result of the interplay between sublimation and mass movement occurring in these regions. Scalloped depressions may have formed during this period because mean obliquity has been lower in the last 5 Ma (Dundas et al., 2015, 2017). Scalloped depressions are a sign of the degradation of volatile materials (Dundas et al., 2017). Based on the distribution results of fan-shaped depression landforms described in Section 3.1, this landform is observed on the surface of the study area, where the underground structure is visible. This suggests that the material is currently undergoing a degradation process or has experienced it in the past. However, the scalloped depression landform is still present on the surface of the lower area of LDM (Figure 4a(c)). Considering that this lower layer of LDM is extensively covered with DRDs, we hypothesize that the materials in this layer still contain volatile substances. The presence of DRDs does not necessarily indicate the manifestation of volatile substances after complete degradation.

4.3. Origin of DRDs

Our study area also contained three types of DRDs: ellipses, teardrops, and labyrinths, that is, morphologies that may be related to rock abundance (Kessler & Werner, 2003). Furthermore, polygons are superimposed over DRDs, which is consistent with the results reported by Bina and Osinski (2021). Notably, the morphological characteristics of the labyrinth shape and those of the brain-terrain are very similar. In contrast, the DRDs differ from the brain-terrain hosted on the CCF, as it has evident directionality rather than being concentrically distributed. Brain-terrains are closely related to glacial landforms (LVF, LDA, CCF). Although only a small number of DRDs are superimposed on the CCFs, most DRDs appear with LDMs, polygons, and scalloped depressions, and these are thought to have originated from water ice-rich formations that have experienced repeated freezing and thawing. Consequently, both DRD and brain terrain are associated with water ice-rich strata, have similar morphologies, and all occur in northern midlatitudes. The formation of “brain terrain” requires buried glacial ice according to previous model results (Levy et al., 2009). The formation hypothesis of DRD suggests its association with the degradation of icy depositions, similar to the formation of “brain terrain,” but there is currently no evidence of water ice detected by instruments such as SHARAD (Bina & Osinski, 2021). The HiRISE images in the study area show that no DRDs are present on the surface of area A1 in Figure 4, where SHARAD detected subsurface reflectors. However, the highly degraded areas surrounding A1 are almost filled with DRDs and the DRDs are widely distributed in the central UP. In most cases, there will be a transition between elliptic DRDs and labyrinth-shaped DRDs along the perimeter of the LDM, eventually connecting with small polygonal landforms on the surface of the LDM with relatively high elevations. Our results from SHARAD data indicate the presence of a large water ice deposit in area A1 of Figure 4, but no subsurface structure on other lower mesa that have significantly degraded landforms on the surface. These phenomena indicate that DRDs function as significant geomorphological indicators of the degradation of near-surface water ice on the topmost mesa. We conclude that SHARAD detected water ice-rich strata in the center of UP where DRD is widely distributed, which provides support for the hypothesis proposed by Bina and Osinski (2021). We also believe that DRD formation is likely to be related to ice sublimation and LDM degradation. Due to DRD being consistent with the brain-terrain on spatial distribution, the ellipse and teardrop shapes do not rule out representing an extension of brain topography. In this area, the scalloped shape is superimposed on the DRDs, so the presence of DRDs does not indicate that volatile materials have been completely removed. There are only about 10 m between the uppermost mesa and the lower layer fully occupied by DRDs from the MOLA, but SHARAD is not able to detect the underground echo for two possible reasons: (a) Water ice is discontinuous in this area and beyond the instrument's range; or (b) The layer is too thin for the instrument resolution.

5. Conclusions

Subsurface echos have been detected by SHARAD in the center of UP. Echo power shows a low signal loss, consistent with an ice-rich material. A dielectric constant of 2.6–5.4 is estimated, also indicating icy materials. Various periglacial landforms can be found around the studied mesa. Based on the geomorphologic and radar evidence, it can be concluded that the mesas in the studied region belong to LDM. We found that a large number of polygons and scalloped depressions appear on the surface and edge of the LDM, but DRDs only appear in areas far away from the LDM. DRDs and LDMs are connected by polygons, so DRD implies a deeper degree of degradation. The radar results have also provided evidence in support of the origin of DRDs, demonstrating that they are formed as a result of the degradation of LDM. According to the latitude dependence of periglacial landforms, DRDs do not appear at lower latitudes (<35° Lat.), likely due to the sublimation of the surface water ice in the region. In our study, we found CCH similar in morphology to a RMC, which is a type of impact crater formed on pure glacial ice (Kress & Head, 2008). The distribution and diameter statistics of CCH suggest the previously present icy layer in eAb unit, reaching hundreds of meters or even kilometers thick in the center of UP. These ice-rich layered deposits in the center of UP contribute to the mid-latitudinal ice budget on Mars.

Data Availability Statement

All data generated by SHARAD and analyzed during this study are included in this article and its supporting information. All data from periglacial landforms analyzed in this paper are archived on Zenodo (Xu, 2024). SHARAD radar data are archived on the NASA Planetary Data System (Campbell, 2006).

Acknowledgments
We thank the entire SHARAD team for their efforts in acquiring these data and the CO-SHARPS team for the processing boutique. Thanks to NASA for providing the SHARAD, MOLA, and CTX data that are publicly available on the Planetary Data System (PDS). Xiaoting.Xu acknowledges funding from the National Key Research and Development Program (Grant 2021YFA0716100): "Exploration of habitable environments and biosignatures on Mars," China. Yi Xu, Zhuo Han, and HonKuan. Wong is supported by the Science and Technology Development Fund of Macau (Grants 0014/2022/A1, 0021/2024/RIA1, 0158/2024/AFJ), Xu Meng acknowledges funding from the Guangdong Basic and Applied Basic Research Foundation (Grant 2024A1515010934).

References

Bina, A. (2018). The periglacial landscape of Mars: Insight into the 'Decameter-scale Rimmed Depressions' in Utopia Planitia. *Electronic Thesis and Dissertation Repository*. 5739. Retrieved from https://ir.lib.uwo.ca/etd/5739

Bina, A., & Osinski, G. R. (2021). Decameter-scale rimmed depressions in Utopia Planitia: Insight into the glacial and periglacial history of Mars. *Planetary and Space Science*, *204*, 105253. https://doi.org/10.1016/j.pss.2021.105253

Bramson, A. M., Byrne, S., Putzig, N. E., Sutton, S., Plaut, J. J., Brothers, T. C., & Holt, J. W. (2015). Widespread excess ice in Arcadia Planitia, Mars. *Geophysical Research Letters*, *42*(16), 6566–6574. https://doi.org/10.1002/2015gl064844

Buczkowski, D. L., & McGill, G. E. (2002). Topography within circular grabens: Implications for polygon origin, Utopia Planitia, Mars. *Geophysical Research Letters*, *29*(7), 59–61. https://doi.org/10.1029/2001gl014100

Campbell, B. (2006). *MRO MARS SHARAD 5 RADARGRAM V2.0*. NASA Planetary Data System. https://doi.org/10.17189/YB1W-F075

Campbell, B., Carter, L., Phillips, R., Plaut, J., Putzig, N., Safaeinili, A., et al. (2008). SHARAD radar sounding of the Vastitas Borealis Formation in Amazonis Planitia. *Journal of Geophysical Research*, *113*(E12), E12010. https://doi.org/10.1029/2008je003177

Campbell, B. A., & Morgan, G. A. (2018). Fine-scale layering of Mars polar deposits and signatures of ice content in nonpolar material from multiband SHARAD data processing. *Geophysical Research Letters*, *45*(4), 1759–1766. https://doi.org/10.1002/2017gl075844

Chamberlain, M. A., & Boynton, W. V. (2007). Response of Martian ground ice to orbit-induced climate change. *Journal of Geophysical Research*, *112*(E6), E06009. https://doi.org/10.1029/2006je002801

Costard, F. M., & Kargel, J. S. (1995). Outwash plains and thermokarst on Mars. *Icarus*, *114*(1), 93–112. https://doi.org/10.1006/icar.1995.1046

Dundas, C. M., Byrne, S., & McEwen, A. S. (2015). Modeling the development of Martian sublimation thermokarst landforms. *Icarus*, *262*, 154–169. https://doi.org/10.1016/j.icarus.2015.07.033

Dundas, C. M., McEwen, A. S., Chojnacki, M., Milazzo, M. P., Byrne, S., McElwaine, J. N., & Urso, A. (2017). Granular flows at recurring slope lineae on Mars indicate a limited role for liquid water. *Nature Geoscience*, *10*(12), 903–907. https://doi.org/10.1038/s41561-017-0012-5

Fergason, R. L., Laura, J. R., & Hare, T. M. (2017). THEMIS-derived thermal inertia on Mars: Improved and flexible algorithm. In *48th Annual Lunar and Planetary Science Conference* (Vol. 1964, p. 1563).

French, R. H. (2013). *Environmental philosophy and the ethics of terraforming Mars: Adding the voices of environmental justice and ecofeminism to the ongoing debate*. University of North Texas.

Head, J. W., III, Kreslavsky, M. A., & Pratt, S. (2002). Northern lowlands of Mars: Evidence for widespread volcanic flooding and tectonic deformation in the Hesperian Period. *Journal of Geophysical Research*, *107*(E1). 3-1–3-29. https://doi.org/10.1029/2000je001445

Head, J. W., Mustard, J. F., Kreslavsky, M. A., Milliken, R. E., & Marchant, D. R. (2003). Recent ice ages on Mars. *Nature*, *426*(6968), 797–802. https://doi.org/10.1038/nature02114

Ivanov, M. A., Hiesinger, H., Erkeling, G., & Reiss, D. (2014). Mud volcanism and morphology of impact craters in Utopia Planitia on Mars: Evidence for the ancient ocean. *Icarus*, *228*, 121–140. https://doi.org/10.1016/j.icarus.2013.09.018

Jakosky, B. M., Slipski, M., Benna, M., Mahaffy, P., Elrod, M., Yelle, R., et al. (2017). Mars' atmospheric history derived from upper-atmosphere measurements of $^{38}Ar/^{36}Ar$. *Science*, *355*(6332), 1408–1410. https://doi.org/10.1126/science.aai7721

Kessler, M. A., & Werner, B. T. (2003). Self-organization of sorted patterned ground. *Science*, *299*(5605), 380–383. https://doi.org/10.1126/science.1077309

Kreslavsky, M. A., & Head, J. W. (2002). Fate of outflow channel effluents in the northern lowlands of Mars: The Vastitas Borealis Formation as a sublimation residue from frozen ponded bodies of water. *Journal of Geophysical Research*, *107*(E12). 4-1–4-25. https://doi.org/10.1029/2001je001831

Kreslavsky, M. A., & Head, J. W. (2003). North–south topographic slope asymmetry on Mars: Evidence for insolation-related erosion at high obliquity. *Geophysical Research Letters*, *30*(15), 1815. https://doi.org/10.1029/2003gl017795

Kress, A. M., & Head, J. W. (2008). Ring-mold craters in lineated valley fill and lobate debris aprons on Mars: Evidence for subsurface glacial ice. *Geophysical Research Letters*, *35*(23), L23206. https://doi.org/10.1029/2008gl035501

Laura, J., & Fergason, R. L. (2016). Modeling martian thermal inertia in a distributed memory high performance computing environment. In *2016 IEEE International Conference on Big Data (Big Data)* (pp. 2919–2928). IEEE.
Levy, J., Head, J. W., & Marchant, D. R. (2010). Concentric crater fill in the northern mid-latitudes of Mars: Formation processes and relationships to similar landforms of glacial origin. *Icarus*, *209*(2), 390–404. https://doi.org/10.1016/j.icarus.2010.03.036
Levy, J. S., Head, J. W., & Marchant, D. R. (2009). Concentric crater fill in Utopia Planitia: History and interaction between glacial "brain terrain" and periglacial mantle processes. *Icarus*, *202*(2), 462–476. https://doi.org/10.1016/j.icarus.2009.02.018
Malin, M. C., Bell, J. F., III, Cantor, B. A., Caplinger, M. A., Calvin, W. M., Clancy, R. T., et al. (2007). Context camera investigation on board the Mars Reconnaissance Orbiter. *Journal of Geophysical Research*, *112*(E5), E05S04. https://doi.org/10.1029/2006je002808
Malin, M. C., & Edgett, K. S. (2000). Sedimentary rocks of early Mars. *Science*, *290*(5498), 1927–1937. https://doi.org/10.1126/science.290.5498.1927
Mangold, N. (2005). High latitude patterned grounds on Mars: Classification, distribution and climatic control. *Icarus*, *174*(2), 336–359. https://doi.org/10.1016/j.icarus.2004.07.030
McEwen, A. S., Eliason, E. M., Bergstrom, J. W., Bridges, N. T., Hansen, C. J., Delamere, W. A., et al. (2007). Mars reconnaissance orbiter's high resolution imaging science experiment (HiRISE). *Journal of Geophysical Research*, *112*(E5), E05S02. https://doi.org/10.1029/2005je002605
McGill, G. E. (1986). The giant polygons of Utopia, northern Martian plains. *Geophysical Research Letters*, *13*(8), 705–708. https://doi.org/10.1029/gl013i008p00705
McGill, G. E. (1989). Buried topography of Utopia, Mars: Persistence of a giant impact depression. *Journal of Geophysical Research*, *94*(B3), 2753–2759. https://doi.org/10.1029/jb094ib03p02753
McGowan, E. M. (2011). The Utopia/Isidis overlap: Possible conduit for mud volcanism on Mars. *Icarus*, *212*(2), 622–628. https://doi.org/10.1016/j.icarus.2011.01.025
Mellon, M. T., Arvidson, R. E., Marlow, J. J., Phillips, R. J., & Asphaug, E. (2008). Periglacial landforms at the Phoenix landing site and the northern plains of Mars. *Journal of Geophysical Research*, *113*(E3), E00A23. https://doi.org/10.1029/2007je003039
Mellon, M. T., Feldman, W. C., & Prettyman, T. H. (2004). The presence and stability of ground ice in the southern hemisphere of Mars. *Icarus*, *169*(2), 324–340. https://doi.org/10.1016/j.icarus.2003.10.022
Mellon, M. T., & Jakosky, B. M. (1995). The distribution and behavior of Martian ground ice during past and present epochs. *Journal of Geophysical Research*, *100*(E6), 11781–11799. https://doi.org/10.1029/95je01027
Milliken, F. J., Morrison, E. W., & Hewlin, P. F. (2003). An exploratory study of employee silence: Issues that employees don't communicate upward and why. *Journal of Management Studies*, *40*(6), 1453–1476. https://doi.org/10.1111/1467-6486.00387
Moore, H. J., Hutton, R. E., Clow, G. D., & Spitzer, C. R. (1987). *Physical properties of the surface materials at the Viking landing sites on Mars* (Vol. 1389). U.S. Geological Survey.
Mouginot, J., Pommerol, A., Kofman, W., Beck, P., Schmitt, B., Herique, A., et al. (2010). The 3–5 MHz global reflectivity map of Mars by MARSIS/Mars Express: Implications for the current inventory of subsurface H_2O. *Icarus*, *210*(2), 612–625. https://doi.org/10.1016/j.icarus.2010.07.003
Mustard, J. F., Cooper, C. D., & Rifkin, M. K. (2001). Evidence for recent climate change on Mars from the identification of youthful near-surface ground ice. *Nature*, *412*(6845), 411–414. https://doi.org/10.1038/35086515
Nelson, F. E., Anisimov, O. A., & Shiklomanov, N. I. (2002). Climate change and hazard zonation in the circum-Arctic permafrost regions. *Natural Hazards*, *26*(3), 203–225. https://doi.org/10.1023/a:1015612918401
Orgel, C., Hauber, E., van Gasselt, S., Reiss, D., Johnsson, A., Ramsdale, J. D., et al. (2019). Grid mapping the northern plains of Mars: A new overview of recent water-and ice-related landforms in Acidalia Planitia. *Journal of Geophysical Research: Planets*, *124*(2), 454–482. https://doi.org/10.1029/2018je005664
Orosei, R., Rossi, A. P., Cantini, F., Caprarelli, G., Carter, L. M., Papiano, I., et al. (2017). Radar sounding of Lucus Planum, Mars, by MARSIS. *Journal of Geophysical Research: Planets*, *122*(7), 1405–1418. https://doi.org/10.1002/2016je005232
Parker, T. J., Gorsline, D. S., Saunders, R. S., Pieri, D. C., & Schneeberger, D. M. (1993). Coastal geomorphology of the Martian northern plains. *Journal of Geophysical Research*, *98*(E6), 11061–11078. https://doi.org/10.1029/93JE00618
Parker, T. J., Saunders, R. S., & Schneeberger, D. M. (1989). Transitional morphology in west Deuteronilus Mensae, Mars: Implications for modification of the lowland/upland boundary. *Icarus*, *82*(1), 111–145. https://doi.org/10.1016/0019-1035(89)90027-4
Pechmann, J. C. (1980). The origin of polygonal troughs on the northern plains of Mars. *Icarus*, *42*(2), 185–210. https://doi.org/10.1016/0019-1035(80)90071-8
Porcello, L. J., Jordan, R. L., Zelenka, J. S., Adams, G. F., Phillips, R. J., Brown, W. E., et al. (1974). The Apollo lunar sounder radar system. *Proceedings of the IEEE*, *62*(6), 769–783. https://doi.org/10.1109/proc.1974.9517
Salvatore, M. R., & Christensen, P. R. (2014). Evidence for widespread aqueous sedimentation in the northern plains of Mars. *Geology*, *42*(5), 423–426. https://doi.org/10.1130/g35319.1
Schon, S. C., Head, J. W., & Fassett, C. I. (2012). An overfilled lacustrine system and progradational delta in Jezero crater, Mars: Implications for Noachian climate. *Planetary and Space Science*, *67*(1), 28–45. https://doi.org/10.1016/j.pss.2012.02.003
Schorghofer, N., & Forget, F. (2012). History and anatomy of subsurface ice on Mars. *Icarus*, *220*(2), 1112–1120. https://doi.org/10.1016/j.icarus.2012.07.003
Seibert, N. M., & Kargel, J. S. (2001). Small-scale Martian polygonal terrain: Implications for liquid surface water. *Geophysical Research Letters*, *28*(5), 899–902. https://doi.org/10.1029/2000gl012093
Séjourné, A., Costard, F., Swirad, Z. M., Łosiak, A., Bouley, S., Smith, I., et al. (2019). Grid mapping the Northern Plains of Mars: Using morphotype and distribution of ice-related landforms to understand multiple ice-rich deposits in Utopia Planitia. *Journal of Geophysical Research: Planets*, *124*(2), 483–550. https://doi.org/10.1029/2018je005665
Seu, R., Phillips, R. J., Biccari, D., Orosei, R., Masdea, A., Picardi, G., et al. (2007). SHARAD sounding radar on the Mars Reconnaissance Orbiter. *Journal of Geophysical Research*, *112*(E5), E05S05. https://doi.org/10.1029/2006je002745
Skinner, J. A., Jr., Tanaka, K. L., & Platz, T. (2012). Widespread loess-like deposit in the Martian northern lowlands identifies Middle Amazonian climate change. *Geology*, *40*(12), 1127–1130. https://doi.org/10.1130/g33513.1
Soare, R. J., Osinski, G. R., & Roehm, C. L. (2008). Thermokarst lakes and ponds on Mars in the very recent (late Amazonian) past. *Earth and Planetary Science Letters*, *272*(1–2), 382–393. https://doi.org/10.1016/j.epsl.2008.05.010
Squyres, S. W. (1978). Martian fretted terrain: Flow of erosional debris. *Icarus*, *34*(3), 600–613. https://doi.org/10.1016/0019-1035(78)90048-9
Squyres, S. W. (1979). The distribution of lobate debris aprons and similar flows on Mars. *Journal of Geophysical Research*, *84*(B14), 8087–8096. https://doi.org/10.1029/jb084ib14p08087
Stillman, D. E., Grimm, R. E., & Dec, S. F. (2010). Low-frequency electrical properties of ice−silicate mixtures. *The Journal of Physical Chemistry B*, *114*(18), 6065–6073. https://doi.org/10.1021/jp9070778

Stuurman, C. M., Osinski, G. R., Holt, J. W., Levy, J. S., Brothers, T. C., Kerrigan, M., & Campbell, B. A. (2016). SHARAD detection and characterization of subsurface water ice deposits in Utopia Planitia, Mars. *Geophysical Research Letters*, *43*(18), 9484–9491. https://doi.org/10.1002/2016gl070138

Szocik, K., Lysenko-Ryba, K., Banaś, S., & Mazur, S. (2016). Political and legal challenges in a Mars colony. *Space Policy*, *38*, 27–29. https://doi.org/10.1016/j.spacepol.2016.05.012

Tanaka, K. L., Robbins, S. J., Fortezzo, C. M., Skinner, J. A., Jr., & Hare, T. M. (2014). The digital global geologic map of Mars: Chronostratigraphic ages, topographic and crater morphologic characteristics, and updated resurfacing history. *Planetary and Space Science*, *95*, 11–24. https://doi.org/10.1016/j.pss.2013.03.006

Tanaka, K. L., Skinner, J. A., & Hare, T. M. (2005). Geologic map of the northern plains of Mars.

Ulrich, M., Morgenstern, A., Günther, F., Reiss, D., Bauch, K. E., Hauber, E., et al. (2010). Thermokarst in Siberian ice-rich permafrost: Comparison to asymmetric scalloped depressions on Mars. *Journal of Geophysical Research*, *115*(E10), E10009. https://doi.org/10.1029/2010je003640

Werner, S. C., & Tanaka, K. L. (2011). Redefinition of the crater-density and absolute-age boundaries for the chronostratigraphic system of Mars. *Icarus*, *215*(2), 603–607. https://doi.org/10.1016/j.icarus.2011.07.024

Wordsworth, R., Forget, F., Millour, E., Head, J. W., Madeleine, J. B., & Charnay, B. (2013). Global modelling of the early martian climate under a denser CO_2 atmosphere: Water cycle and ice evolution. *Icarus*, *222*(1), 1–19. https://doi.org/10.1016/j.icarus.2012.09.036

Xu, X. (2024). Periglacial landforms [Dataset]. *Zenodo*. https://doi.org/10.5281/ZENODO.10018815

Zou, Y., Zhu, Y., Bai, Y., Wang, L., Jia, Y., Shen, W., et al. (2021). Scientific objectives and payloads of Tianwen-1, China's first Mars exploration mission. *Advances in Space Research*, *67*(2), 812–823. https://doi.org/10.1016/j.asr.2020.11.005